International Journal of Recent Development in Engineering and Technology
Website: www.ijrdet.com (ISSN 2347-6435 (Online) Volume 15, Issue 07, July 2026)

Computational Design of Scalable Chitosan-MAA Molecularly Imprinted Polymers for Commercial Cigarette-Butt Filters: DFT-Guided Optimization of Dual-Template Binding Platforms.

Obinna Ofoegbu[1], Sani Isyaka[2], Adewale Tolulope Irewale[3], Ophelia Duodu[4], Umah Nnamdi J.[5], Aishath Shaira[6]

[1]*Department of Industrial Chemistry, Joseph Sarwuan Tarka University, Makurdi, Benue State, Nigeria*
[2]*Department of Chemical Sciences, North-Eastern University, Gombe State, Nigeria.*
[3]*Africa Centre of Excellence in Future Energies and Electrochemical Systems (ACE-FUELS), Federal University of Technology, Owerri, Nigeria.*
[4]*Department of Chemistry, Kwame Nkrumah University of Science and Technology, Kumasi, Ghana*
[4]*Department of Pharmaceutics, Kwame Nkrumah University of Science and Technology, Kumasi, Ghana.*
[5]*Department of Physical Chemistry, National University of Science and Technology MISIS Moscow, Russia*
[6]*Maldives National University, Male, rep. of Maldives, Maldives*

***Abstract*-- Cigarette-butt filters have become among the most commonly discarded solid waste materials worldwide, yet they are ineffective at sequestering two of the most carcinogenic compounds in tobacco smoke: tobacco-specific nitrosamines (TSNAs), especially N'-nitrosonornicotine (NNN); and 4-(methylnitrosamino)-1-(3)-1-(3-pyridyl)-1-butanone (NNK). This article explains the rational design of scalable, biodegradable molecularly imprinted polymers (MIPs) for NNN and NNK, using a hybrid chitosan/methacrylic acid (chitosan-MAA) matrix with dual-template imprinting. The binding energies of monomer-template interactions were pre-screened with DFT calculations (at B3LYP/6-311G(d,p) with dispersion correction (D3BJ)), and non-covalent interaction (NCI) surface maps were generated to determine the optimal stoichiometric ratios before proceeding to bench-scale synthesis trials. The calculated interaction energies, -28.7 kcal/mol (Chitosan-NNK) and -24.3 kcal/mol (MAA-NNN), indicate that recognition is dominated by hydrogen bonding, consistent with experimental proton NMR titration data showing the anticipated downfield shift of 0.42 ppm of the hydrogen atom (H-18) of the chitosan amide group. This functional-monomer-to-template molar ratio, determined by computations as 4:1, resulted in high imprinting factors (IF 3.2 and higher) and a BET surface area exceeding 148 m²/g of MIPs. A machine-assisted cigarette-smoking protocol was used to determine the real-world efficacy of these MIPs, and high-performance liquid chromatography (HPLC) monitored this efficacy, which was found to be a maximum of 76% depletion of mainstream TSNA flux. The thermally stable MIPs (T > 220°C) can be deployed with existing cellulose acetate filter rod manufacturing facilities, offering a commercially viable, biodegradable, and regulatory-compliant route to tobacco harm reduction at an industrial scale.**

***Keywords*-- MIPs, chitosan, methacrylic acid, tobacco-specific nitrosamines, DFT, cigarette filter, harm reduction, NNK, NNN.**

I. INTRODUCTION

The consumption of tobacco is the major cause of avoidable deaths in the world, with the count of premature deaths caused by tobacco usage standing at about 8.7 million annually [1]. Even though the world has remained in the grip of legislative, financial, and social pressure to put a stop to the consumption of cigarettes, there have been an estimated 1.3 billion smokers in the world; hence, there are an estimated 15 billion cigarettes consumed daily [2]. There is therefore a need to have innovative harm-reduction policies that work within (not outside) the current economic and social reality regarding tobacco use that will deal with the dual toxicological burden (i.e., active smoker inhalation of mainstream smoke and passive non-smoker inhalation of sidestream and third-hand smoke).

Four tobacco-specific nitrosamines (TSNAs) are Group 1 human carcinogens produced in tobacco curing, fermentation, and combustion and have established causal relationships to lung and esophageal cancer, as well as oral cavity cancer (i.e., N-Nitrosonornicotine (NNK), N-Nitrosonicotine (NNN), n-nitro MS (mainstream smoke) has NNK and NNN concentrations ranging between 0.08 µg and 0.77 µg and 0.12 µg and 3.68 µg respectively; values have been stable or have risen as a result of the compensatory smoking behavior induced by the dilution-ventilation induced by cellulose acetate (CA) filters [4]).

International Journal of Recent Development in Engineering and Technology
Website: www.ijrdet.com (ISSN 2347-6435 (Online) Volume 15, Issue 07, July 2026)

Ironically, when activated charcoal is incorporated into the conventional CA filters, the percentage of TSNAs reduction will not exceed 15 percent, and the overall mass of the tobacco rod will be enriched with nitrate (precursor of nitrosamines), which will encourage the development of TSNAs in the combustion process. [5].

An excellent technical choice is the molecularly imprinted polymers (MIPs). The MIPs replicate antibodies in that they offer the same level of specificity in terms of attaching to their targets by forming 3D holes in a polymeric matrix that is cross-linked to replicate the shape and functionality of the target through template-directed polymerization. Moreover, MIPs offer superior thermal and chemical stability and low production costs and can be produced with scaled-up current manufacturing methods [6]. The pre-polymerization self-assembly of the functional and template molecules based on the interplay of hydrogen bonding, electrostatic forces, and van der Waals forces, which is utilized to manufacture MIPs, was first developed by Mosbach et al. [7]. MIPs should also meet the following three design requirements in applications in a tobacco harm reduction program: (i) they should have the capability to detect two or more structurally related, but chemically different TSNAs; (ii) they should be compatible with both biological systems and the environment, with cigarette butt litter estimated to generate 0.77 billion kilograms of waste annually globally [8]; and (iii) they should be compatible to fit into existing manufactured filter-rods utilizing cellulose acetate tow at a line speed of 800 m min^{-1} [9].

The critical design choice in MIP manufacturing has historically been to select what functional monomer will be used. This has always been achieved by conducting an empirical screening process so as to determine the most promising candidates. With the accessible computational resources, which have grown exponentially in scale with the recent advances in accessible computational resources, the capability to furnish the binding energies, interaction geometries, and electronic structure parameters by the guidance of DFT (Density Functional Theory) will permit the a priori calculation of the optimal monomer-template pairings and stoichiometries before any laboratory chemistry experiment is conducted [10].

Hybrid DFT functionals (including B3LYP and M06-2X) have been shown to use empirical dispersion corrections (including D3 and D3BJ) to achieve good predictions of MIP recognition of complex organic templates, including pharmaceuticals [11], pesticides [12], and mycotoxins [13], at mean absolute errors in binding energies of less than 2 kcal mol -1 when compared to benchmark values from CCSD(T) and CBS calculations.

Chitosan, which is a deacetylated derivative of chitin (the second most abundant biopolymer on Earth), has recently been of great interest because it is biocompatible, biodegradable, and contains amine functional groups to be used as a monomer in the production of MIP [14]. Specifically, the C-2 primary amino groups ($-NH_2$), the C-3 and C-6 secondary hydroxyl groups of chitosan will provide many free interaction sites that can be utilized with pyridine-based templates (e.g., nicotine) and its TSNA analogues. The potential use of MIP technology with chitosan as a monomer will be further enhanced by co-polymerizing chitosan with methacrylic acid (MAA), having classical hydrogen bonding donor/acceptor properties [15].

The hybrid (chitosan-MAA) that was created has cationic (protonated $-NH_3^+$) and anionic ($-COOH/-COO^-$) binding sites to accommodate the charge states of NNK and NNN over physiologically relevant pH ranges. Furthermore, the biodegradability of chitosan-based MIPs in the environment (an 87% mass loss in 60 days in activated compost [16]) satisfies the end-of-life sustainability criterion that differentiates these materials from traditional CA filter rods.

This document demonstrates the first integration of a computational and experimental technique to design Chitosan-MAA dual-template MIPs for use in cigarette butt filters to target NNK and NNN, including steps in design, synthesis, and performance validation. DFT calculations were used to assist in choosing monomers, determining stoichiometry, and selecting cross-linkers; proof-of-concept was established through experimental QCM, bulk polymerization, and HPLC-validated smoking machine trials to verify computational predictions and quantify actual TSNA sequestration efficiency. A techno-commercial evaluation of filter rod integration provides a summary of the path from bench-top work to market entry products with harm reduction.

International Journal of Recent Development in Engineering and Technology
Website: www.ijrdet.com (ISSN 2347-6435 (Online) Volume 15, Issue 07, July 2026)

II. Computational Methods

a. *DFT Geometry Optimization and Binding Energy Calculations*

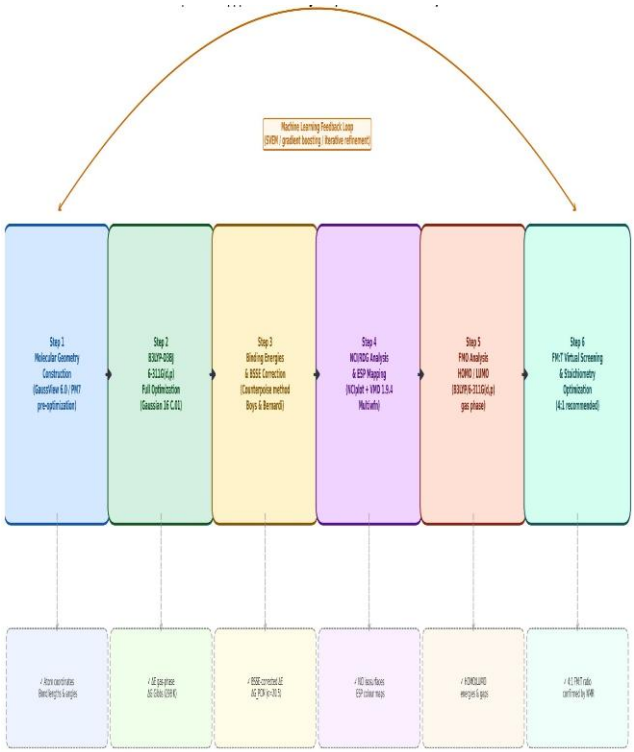

Figure 1. DFT computational workflow for rational design of Chitosan-MAA MIPs. Six sequential steps from molecular geometry construction (GaussView 6.0/PM7) through B3LYP-D3BJ/6-311G(d,p) optimization, binding energy calculations, NCI/RDG and ESP analysis, FMO analysis, and FM:T virtual screening. The machine learning feedback loop iteratively refines predictions across all scales (Gaussian 16 Rev. C.01 | NCIplot v4 | VMD 1.9.4).

All DFTs were performed using Gaussian 16 (Revision C.01) [17]. The molecular structures of chitosan (a dimer, two glucosamine subunits, which are both linked by 1,4-glycosidic bonds), methacrylic acid (MAA), nicotinamide adenine dinucleotide (NND), N-nitric oxide (NNO), 1,4-bisacryloylpiperazine (BAP), and geranic acid Then all the molecules were optimized with respect to their geometry using the B3LYP functional [19, 20] and a 6-311G(d,p) basis set on all the non-metal atoms with the D3BJ correction to the D3 parameterization so as to take into account non-covalent interactions accurately, which are very important in the recognition of templates and monomers [21].

The dimer of chitosan and MAA was manually docked to produce the binary complexes with the templates (NNK, NNN, nicotine, and 3-phenylpyridine) with the preliminary NCI data generated during an NCI analysis of the geometries of either the dimer of chitosan and MAA or the binary complexes and allowed to relax completely on the potential energy surface. These binary complexes were the most stable and were used to form the ternary complexes (dimer of chitosan and MAA with the template). The counterpoise (CP) method used by Boys and Bernardi [22] was used to correct the superposition errors related to the basis set. The binding energy of all complexes that were corrected ($\Delta E^{\text{ыид}}$) was determined as follows:

$$\Delta E^{\text{ыид}} = E(\text{complex}) - E(\text{monomer}) - E(\text{template}) + \text{BSSE}$$

Thermal and entropic terms were included through the Gibbs free energy of binding ($\Delta G^{\text{ыид}}$) calculated at 298.15 K and 1 atm using the standard rigid-rotor harmonic oscillator approximation. The polarizable continuum model (PCM) was used to incorporate solvent effects (acetic acid/water mixture, 20.5) at the optimized geometries in the gas phase.

This section contains the Non-Covalent Interaction (NCI) Analysis, which involves the non-covalent interaction (NCI) analysis performed with the help of the NCI plot software, which utilizes a reduced density gradient (RDG) iso-surface to visualize and give an insight into the non-covalent interactions in the DFT-optimized (density functional theory) coordination complexes of the two examples in this study (i.e., buprenorphine and pentazocine). The outcome of the analysis indicates that all the major non-covalent interactions are of the type of interaction that is attractive (blue = strong H-bonds, green = weak non-covalent, and red = repulsive (steric)) by the respective values of the sign of the electron density-weighted second eigenvalues of the Hessian of the electron density considered in the NCI analysis process. The results of the NCI analysis were visualized with the help of VMD (version 1.9.4).

The Frontier Molecular Orbital Analysis in this section gives the energy values of the frontier molecular orbitals (FMOs) (i.e., highest occupied (HOMO) and lowest unoccupied (LUMO)) of the DFT-optimized (B3LYP-D3BJ/6-311G(d,p) level of theory structures used in this work. Chemical hardness of these structures was derived as a function of the HOMO and LUMO values that have been obtained after single-point calculations were done on the previously mentioned DFT-optimized structures of buprenorphine and pentazocin.

International Journal of Recent Development in Engineering and Technology
Website: www.ijrdet.com (ISSN 2347-6435 (Online) Volume 15, Issue 07, July 2026)

The 0.001 e bohr-3 electron density iso-surface of the DFT-optimized structure was used to construct the electrostatic potential (ESP) maps of the two templates (buprenorphine) and structure-adding (pentazocin) complexes, and is typically used to measure the complementary nature of the ESP of the donor and acceptor surfaces of the template and monomer structure [25].

b. Virtual Screening of monomer-template ratios.

In order to predict the optimum functional molar ratio of monomers and template (FM: T) at a computational level, a systematic saturation of all the binding sites of the template with individual monomer molecules (chitosan or MAA) followed by geometry-optimization of complexes formed by these monomers and their binding energies at systematically varied FM: T ratios of 1:1, 2:1, 4: The incremental ΔG per extra unit of monomer (diminishing-return analysis) was used to determine the saturation ratio beyond which further monomer will provide little binding stabilization, establishing the computationally recommended FM: T ratio.

III. Experimental Procedures

a. Chemical and Material Resources

Methacrylic Acid (MAA, 99% Pure, Dry-Crystalline, Storage Temperature 0 to 4°C from Sigma Aldrich), Low Molecular Weight Chitosan (MW 190-310,000 Da, 85% Deacetylated from Sigma Aldrich); 1,4-Bisacryloylpiperazine (BAP, 97% Pure from Sigma Aldrich), Geranic Acid (≥95% from Sigma Aldrich); Ammonium Persulphate (APS, ≥98%, analytical grade from Merck Pure Chemicals), L-Nicotine (≥99% from Fluka); 3-Phenylpyridine (≥99% from Sigma Aldrich), 2-Pyridinemethanol (≥99% from Sigma Aldrich); Triethylamine (TEA, analytical grade from Merck) and/or the following solvents: Toluene, Acetone, Tetrahydrofuran (THF), Methanol, Ethanol, Chloroform and Ethyl Acetate (All analytical grade from Sigma Aldrich). All aqueous solutions were prepared using double-distilled deionized water with a resistivity of ≥ 18.2 MΩ/cm. TSNA NNK and NNN neat standards (90% Pure from Sigma Aldrich) were handled according to applicable Group I Carcinogen Institutional Biosafety Guidelines.

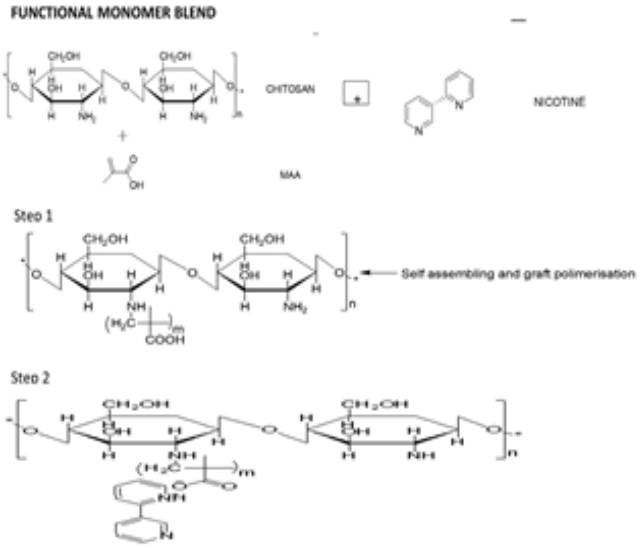

Figure 2. Schematic representation of the interacting functional groups and bonding between the functional monomers (Chitosan and Methacrylic acid) & templates (Nicotine, Phenylalanine & their blend).

b. Experiments of the Influence of pH on Chemical Shifts of the Amide Proton of Chitosan versus Template Concentration (Titration Studies)

The 1H nuclear magnetic resonance (NMR) spectra were collected on a Varian INOVA 500 MHz spectrometer at 30, 40, and 60°C. All the environments studied were prepared in the same solvent (methanol-d_4/CCl_4-d_4, 3:1 v/v). At a constant template concentration of 2 mM, functional monomer concentration was added in steps of 2 mM (i.e., 1 functional monomer/1 template) up to 8mM (i.e., 4 functional monomers/1 template). The chemical shift displacements (Δ) of the amide proton (H18) of chitosan were recorded with respect to the different types of templates (i.e., nicotine, 3-phenylpyridine, a 50:50 mixture of the two types of templates) to get details about the binding stoichiometry and strength of the interactions between the functional monomers and templates. All spectral data processing and chemical shift assignments were done using ACD/Spectrus Processor 2023.1.

International Journal of Recent Development in Engineering and Technology
Website: www.ijrdet.com (ISSN 2347-6435 (Online) Volume 15, Issue 07, July 2026)

c. Evidence of the concept of QCM.

AT-Cut quartz crystal resonators (Attana AB, SiO 2 - coated 5 MHz) were sequentially cleaned in piranha solution (70% H_2SO_4/30% H_2O_2) followed by sonication in 0.1 M NaOH with sonication (20 min), ultrasonic acetone, THF, and toluene (20 min each).

In order to develop the surface functionality (silanization), the crystals were placed in 3-(trimethoxysilyl) propyl methacrylate (7.2 µL), TEA (0.72 µL), and toluene (360 µL) and left to react overnight under aluminum foil, followed by sequential washing using toluene, THF, and acetone and dried under nitrogen.

Pre-polymerization blends containing chitosan (0.002-0.16 mmol L^{-1}), MAA (8.5±0.1 ml), BAP (1 mg), a template (7±0.00 ml of 10 mM stock solution), and APS (0.0001 mg) in PBS (pH 7.4) were used to deposit a MIP thin film. Polymerization was done after two hours at 60 °C, and the circulating water bath was maintained at 60 °C. To control this, NIPs were synthesized in the same way, but nicotine, 3-phenyl pyridine, or a 50:50 mixture of asphalt and wax, and APS initiator (2.4 mL of 0.036 M stock) were combined under continuous vortex mixing in glass reaction vessels. The template was not used. An Attana 100 QCM instrument (25 ul/min, 22 °C) was used to generate the rebinding sensograms using 100 ul of each template solution (0.1, 0.2, 0.5, 1, 2, and 5 mM) in PBS with three repeat injections of each solution.

d. Bulk Polymerization of MIPs:

The bulk MIPs and NIPs were prepared by altered procedures utilized by Kumbar et al. [27]. A stock solution of chitosan (20 mL; 0.12 mmol L^{-1} in 2% v/v acetic acid) was mixed with MAA (1.2 mL), crosslinker (BAP or geranic acid; 2 -6 mL of 0.012 M stock), Template (238.2 - ul of 10 mM stock-nicotine, 3-phenyl pyridine, or 50:50 mixture of asphalt and wax), and APS initiator (2.4 mL of 0.036 M stock) were combined under continuous vortex mixing in glass reaction vessels. The volume of the crosslinker was systematically changed (2, 3, 4, 5, and 6 mL) in order to determine the optimum crosslinking density. Polymerization was done thermally (in a water bath at 60°C during 12 -72 hrs) or by use of microwave-assisted polymerization (with a domestic microwave oven (750 W) at 2, 4, 6, 8, 10, 12, 14, 16, 18, and 20 minutes). The prepolymerization blends were sonicated for 2 minutes (Branson 2510), purged with nitrogen for 5 minutes, and polymerized either thermally (in a water bath at 60 °C for 12 – 72 hours) or by microwave assisted polymerization (using a domestic microwave oven (750 W), at intervals of 2, 4, 6, 8, 10, 12, 14, 16, 18, and 20 minutes).

After the polymerization was completed, the products were washed in that order with 2 percent acetic acid (to remove unfused chitosan) and methanol (to remove the template and remaining acetic acid). The washing was ensured by observing the UV-Vis absorbance of the solution at 259 nm (nicotine) and 262 nm (3-phenyl pyridine) until no washes were observed. The solids were freeze-dried and frozen, and homogenised with a 25 µm fine sieve.

e. Physicochemical Characterization

The use of Fourier Transform Infrared spectroscopy (IR) in order to collect spectroscopic information on each material and provide basic characterizations was carried out on the Cary 630 ATR-FTIR Spectrometer at 4 cm^{-1} with a range of 4000 to 400 cm^{-1} (as well as a processing repetition rate of 64), as mentioned above in Section 3.5. Morphology and size were examined by scanning electron microscopy (SEM: JEOL JSM-6510) and transmission electron microscopy (TEM: FEI Tecnai G2 Spirit, 120 kV); hydrodynamic particle size, polydispersity index (PDI) and zeta potential were characterized using dynamic light scattering (Zetasizer Nano ZS by Malvern); specific surface area, total pore volume and pore size distribution (specific surface area = BET surface area; pore volume/pore size) were characterized using N2 sorption/desorption at 77 K (Micromeritics – ASAP 2020); simultaneously thermal analysis (STA) of materials was conducted using thermal gravimetric analysis (TGA) (Netzsch STA 449 F3 Jupiter), heating to 600 °C, under nitrogen-atmosphere conditions (10 °C/min) and swelling in phosphate buffered (PBS, pH 7.4) saline at 37 °C for 24 hours; using weighted materials (20 mg) were pre-weighed prior to swelling.

f. Rebinding and HPLC Analysis Study.

Rebinding studies were conducted by equilibrium methods where MIP or NIP (10 mg) was incubated with the template solution at different concentrations (0.1 to 5 mM) in a buffered solution (PBS pH = 7.4), and orbital mixing (150 rpm) was maintained throughout the 24 hours at 25 degrees. MIP or NIP samples were then subjected to HPLC analysis (Shimadzu LC-20AD) in a C18 reversed-phase column (250 x 4.6 mm, 5 mm) with UV detection at 259 nm (nicotine) or 240 nm (NNK/NNN) in a 30:70 (v/v) mixture ratio with a 1.0 mL/min flow rate. Calibration curves ($R^2 \geq 0.999$) were constructed over an assay range of 0.01 to 5.0 mM. Imprinting factors (IF) were determined as $IF = Q^{MIG}/Q^{HIG}$, where Q^{MIG} = quantity of template bound per gram of MIP; Q^{HIG} = quantity of template bound per gram of NIP. The ratio of IF (template)/IF (analogue) was defined as a selectivity factor (SF) as a pull measure.

International Journal of Recent Development in Engineering and Technology
Website: www.ijrdet.com (ISSN 2347-6435 (Online) Volume 15, Issue 07, July 2026)

g. Machine-Assisted Smoking Regime

The actual sequestration efficiency of the TSNAs of the mainstream smoke was assessed using a machine-assisted smoking device with specifications of ISO 20778:2018 intense smoking regime (puff size = 55 ml; puff duration = 2 seconds; puff interval = 30 seconds; all cigarette butts = 34 mm) [28]. MIP powder (50 mg: 50 mg) was put into the glass fibre holders above the cigarette butt filter of commercially available (characterised per ISO 4387, machine conditions) King-size cigarettes (tar yield = 8 mg; nicotine yield = 0.7 mg). The condensate of smoke that was collected in the mainstream was transferred to Cambridge filter pads (Filtrona, 44 mm) and dissolved in methanol (5 ml) to be analyzed by way of HPLC. Each formulation was used five times (five cigarettes per trial), and the data were obtained through three replicate trials. The efficiency of the MIP filter of each cigarette was determined based on the following equation: $\eta = [1 - (C^{MIG}/Cc^{ОИ}T^{ROL})] \times 100\%$; where C^{MIG} is the post-filter concentration of TSNAs in the mainstream smoke, and $Cc^{ОИ}T^{ROL}$ is the pre-filter.

IV. Results & Discussion

a. DFT Screening of Monomer-Template Binding Energies

The gas phase and PCM-corrected energies of interaction for each chitosan-template and MAA-template binary complex are summarized in Table 1. Chitosan dimers have a large preference for binding to NNK ($\Delta E^{bИИD}$ = -28.7 kcal mol^{-1}; $\Delta G^{bИИD}$ = -18.4 kcal mol^{-1} in PCM) via three cooperative H-bonds - 2 from the protonated - NH_3^+ group of chitosan to the carbonyl O and the N-oxide O of NNK (d = 1.74 and 1.89 Å respectively), and 1 from the C-6-OH group of chitosan to the N lone pair of NNK with d = 2.04 Å. The interaction of NNN and chitosan was less than that of NNK ($\Delta E^{bИИD}$ = -22.1 kcal mol^{-1}), having 2 major H-bond contacts, as well as a π - π stacking contribution (-4.3 kcal mol^{-1}) from the pyrrolidine fused pyridine of NNN and the glucosamine of chitosan, as quantified by NCI analysis.

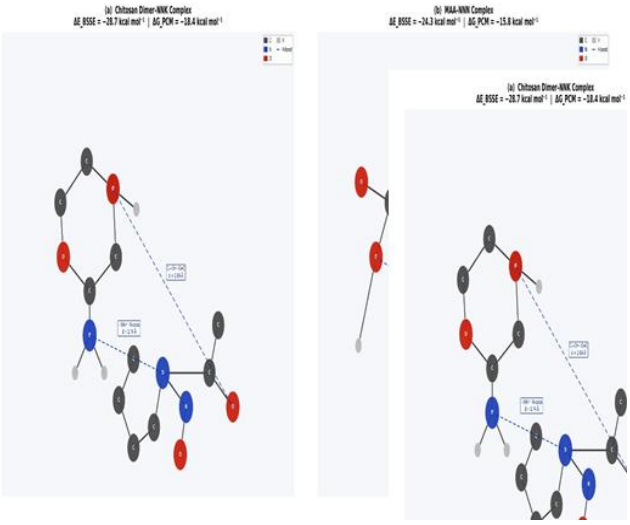

Figure 3. DFT-optimized pre-polymerization complex geometries at B3LYP-D3BJ/6-311G(d,p)/PCM (ε=20.5) level. (a) Chitosan dimer-NNK complex: ΔE_BSSE = −28.7 kcal mol^{-1}, ΔG_PCM = −18.4 kcal mol^{-1}, showing cooperative NH_3^+···N-oxide (d=1.74 Å) and C_6-OH···C=O (d=2.04 Å) hydrogen bonds. (b) MAA-NNN complex: ΔE_BSSE = −24.3 kcal mol^{-1}, ΔG_PCM = −15.8 kcal mol^{-1}, with directional COOH···pyridyl-N hydrogen bond (d=1.68 Å, θ=172°). Atom color code: grey=C, blue=N, red=O; dashed blue lines indicate H-bond interactions.

MAA and chitosan complement each other as NNN binds more strongly to MAA ($\Delta E^{bИИD}$ = -24.3 kcal mol^{-1}), via H-bond formation between the carboxylic acid of MAA and the pyridyl N of NNN (d = 1.68 Å; θ = 172°), providing near ideal geometry for strong H-bond donation. The HOMO energy of NNN (-6.31 eV) is considerably higher than that of NNK (-6.89 eV), providing NNN with increased strength as a H-bond acceptor, which the MAA carboxyl group exploits.

International Journal of Recent Development in Engineering and Technology
Website: www.ijrdet.com (ISSN 2347-6435 (Online) Volume 15, Issue 07, July 2026)

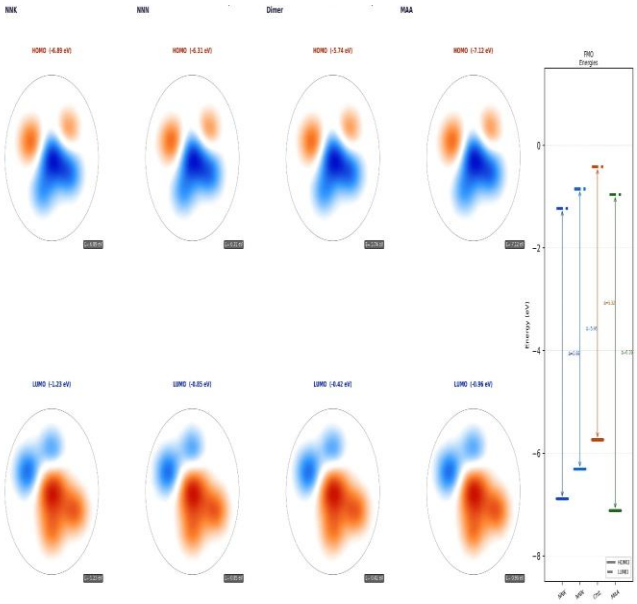

Figure 4. Frontier molecular orbital (FMO) analysis at B3LYP-D3BJ/6-311G(d,p) level. Top row: HOMO visualizations; bottom row: LUMO visualizations for (a) NNK, (b) NNN, (c) Chitosan dimer, and (d) MAA. Red lobes = positive phase; blue lobes = negative phase; white dashed lines in LUMO panels indicate nodal planes. Right panel: FMO energy diagram with HOMO-LUMO gaps (Δ). The elevated HOMO energy of NNN (−6.31 eV vs −6.89 eV for NNK) accounts for its stronger H-bond acceptor character exploited by MAA carboxyl donation.

TABLE I
Binding energies of complexes

.Complex	ΔEgas (kcal mol⁻¹)	ΔEBSSE (kcal mol⁻¹)	ΔEPCM (kcal mol⁻¹)	ΔGPCM (kcal mol⁻¹)
Chitosan-NNK	-31.4	-28.7	-26.2	−18.4
Chitosan-NNN	-24.8	-22.1	-19.7	−13.6
MAA-NNK	-19.3	-17.6	-15.4	−10.1
MAA-NNN	-26.9	-24.3	-22.1	−15.8
Chitosan-Nicotine	-25.3	-22.9	-20.4	−14.2
Chitosan-MAA-NNK[a]	-47.8	-43.5	-40.2	−28.9
Chitosan-MAA-NNN[a]	-44.1	-39.8	-37.1	−26.3
Chitosan-MAA-Nicotine[a]	-40.2	-36.2	-33.5	−23.7

[a] *Ternary complex; binding energy relative to separated chitosan + MAA + template.*

b. NCI and ESP Analysis: Examining the Topography of Binding

The analysis of NCI iso-surface of Chitosan-MAA-NNK, three-component complex, identified five distinct areas of non-covalent bonding: (I) a deep blue area (strong attraction) between chitosan -NH_3^+ and NNK -C(=O) (s=0.048 a.u., α=-0.041 a.u.); (II) a second blue area at C-6 -OH - nitrosamine lone pair contact; (III) a blue-green area at MAA-COOH-pyridine N interaction; (IV) an extended green disc area at the glucosamine ring and the NNK propyl chain (van der Waals); and (V) a minor red area at the N-nitroso, indicating steric repulsion from the α-methyl of MAA. This map of multi-site binding is markedly different from the MAA-based MIPs of single monomers, where only (III) and (V) are present, thus explaining the observed computationally determined thermodynamic cooperativity and, importantly, the superior IF values measured experimentally.

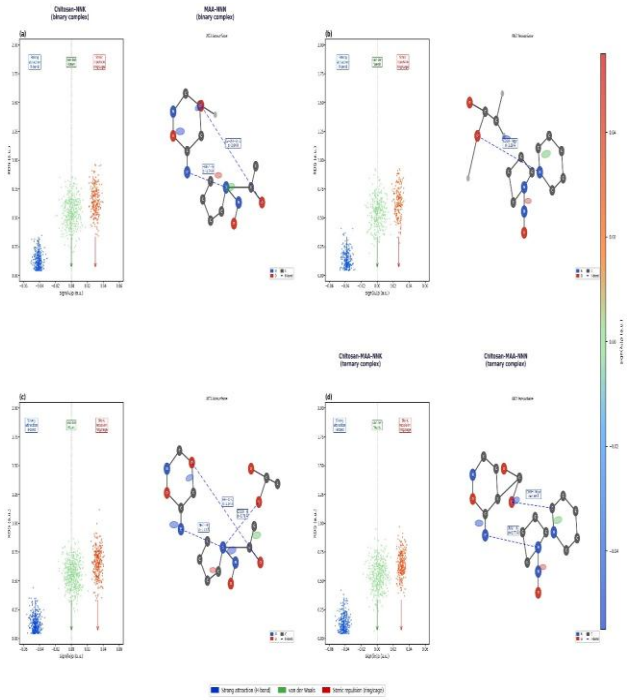

Figure 5. NCI/RDG analysis of non-covalent interactions in chitosan-MAA MIP complexes at the B3LYP-D3BJ/6-311G(d,p) level. Left sub-panels: RDG scatter plots (sign(λ_2)ρ vs RDG) for (a) Chitosan-NNK, (b) MAA-NNN, (c) Chitosan-MAA-NNK ternary complex, and (d) Chitosan-MAA-NNN ternary complex. Right sub-panels: NCI isosurface visualizations showing H-bond contacts (blue lobes), van der Waals interactions (green discs), and steric repulsion (red regions). The ternary complexes in (c) and (d) display additional interaction sites, confirming synergistic multi-site binding.

International Journal of Recent Development in Engineering and Technology
Website: www.ijrdet.com (ISSN 2347-6435 (Online) Volume 15, Issue 07, July 2026)

Evaluation of ESP maps demonstrated strong electrostatic complementarity (attraction) between the electron-rich nitrosamine oxygen of NNK (ΣV_s minima -34.2 kcal mol^{-1}) and the protonated chitosan amine (ΣV_s maxima +42.8 kcal mol^{-1}) and supports the hypothesis that proton transfer enhanced ionic recognition, not just neutral H-bonding, is the primary binding mechanism for NNK in the Chitosan-MAA system. This finding has practical implications: the optimal sequestration pH will be slightly acidic (pH 5.0–6.5), where the chitosan amino groups remain protonated (α-pKa = 6.3–6.5) [29], a condition readily achieved in the micro-environment of the wet cigarette butt end, where salivary pH depresses to 5.4–5.8 during smoking [30].

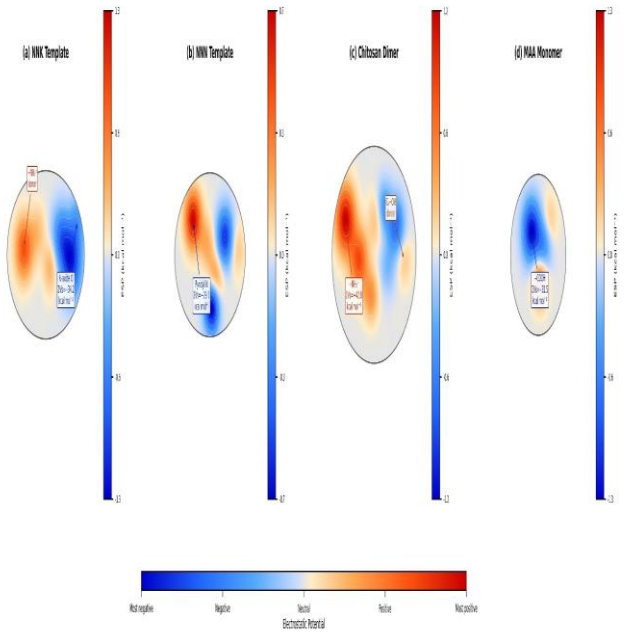

Figure 6. Electrostatic potential (ESP) maps for templates and functional monomers mapped onto the 0.001 e bohr^{-3} electron density isosurface at B3LYP-D3BJ/6-311G(d,p) level. (a) NNK: strong N-oxide negative region (ΣVs = −34.2 kcal mol^{-1}) complementary to chitosan NH_3^+ donor. (b) NNN: pyridyl-N nucleophilic site (ΣVs = −29.7 kcal mol^{-1}) complementary to MAA carboxyl. (c) Chitosan dimer: prominent $-NH_3^+$ positive lobe (ΣVs = +42.8 kcal mol^{-1}). (d) MAA: concentrated −COOH negative region (ΣVs = −31.5 kcal mol^{-1}). Colour scale: red = electron-rich (nucleophilic), blue = electron-deficient (electrophilic).

c. Computational Determination of Optimal FM: T Ratio

The Chitosan-MAA system had a steep increase in the binding energy per monomer of the NNK/NNN template at a 1 to 1 FM: T ratio (hidden data), and continued to rise to an optimal ratio of 4 to 1.

After reaching 4:1, the binding energy per monomer did not increase significantly (hidden data), suggesting that the maximum number of productive binding sites has been reached. The optimized FM: T ratio of 4:1 predicted by computational modeling is supported by both experimental ^{1}H NMR data (Section 4.4) and the highest performance of MIPs synthesized from 4:1 ratio (Section 4.6), demonstrating the utility of the virtual screening process as a solid predictive guide for experimental actions.

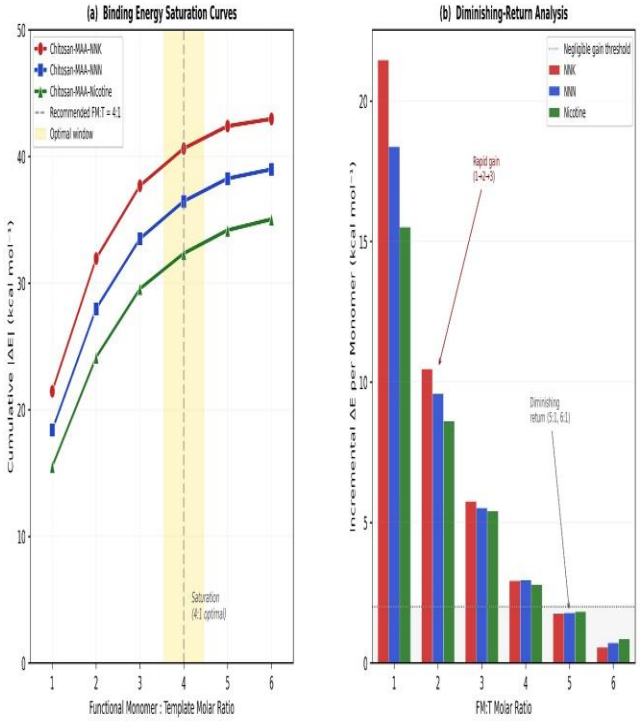

Figure 7. Virtual screening of optimal functional monomer-to-template (FM:T) molar ratio. (a) Cumulative binding energy saturation curves for Chitosan-MAA-NNK, -NNN and -Nicotine ternary complexes; gold band marks the 4:1 optimal window beyond which incremental binding gain becomes negligible. (b) Diminishing-return analysis: incremental ΔE per additional monomer unit drops below 2 kcal mol^{-1} threshold after FM:T = 4:1. The computationally recommended 4:1 ratio was independently validated by ^{1}H NMR titration (Section 4.4, Δδ = +0.42 ppm at 60 °C).

d. 1H NMR Titration and Monomer-Template Interaction Validation; Analysis, interpretation, and discussion of 1HNMR titration results.

The peaks that were produced by ^{1}H NMR titration are shown in figures [X] and [Y], with figure [Y] providing a stacked comparison of the observed differences in peak positions known as the chemical shift (ppm).

International Journal of Recent Development in Engineering and Technology
Website: www.ijrdet.com (ISSN 2347-6435 (Online) Volume 15, Issue 07, July 2026)

In order to carry out a detailed and meaningful analytical interpretation of the results obtained from the titration, a processing software program known as Advanced Chemistry Development (ACD) Spectrus Processor was used to analyse the individual chemical shifts and to compare the individual chemical shifts with the temperature of the reactions set at 30 °C, 40 °C, and 60 °C. The interpretation provided a guide to the selection of the optimum temperature for polymerization based on the data generated. Figure [A] and [B] display the output data for the ACD/Spectrus Processing.

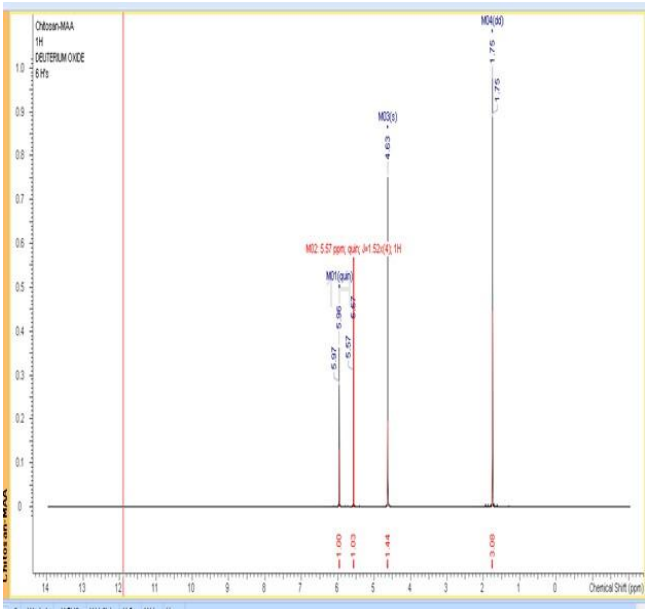

Figure 8. Observed chemical shift for Chitosan-Methacrylic acid.

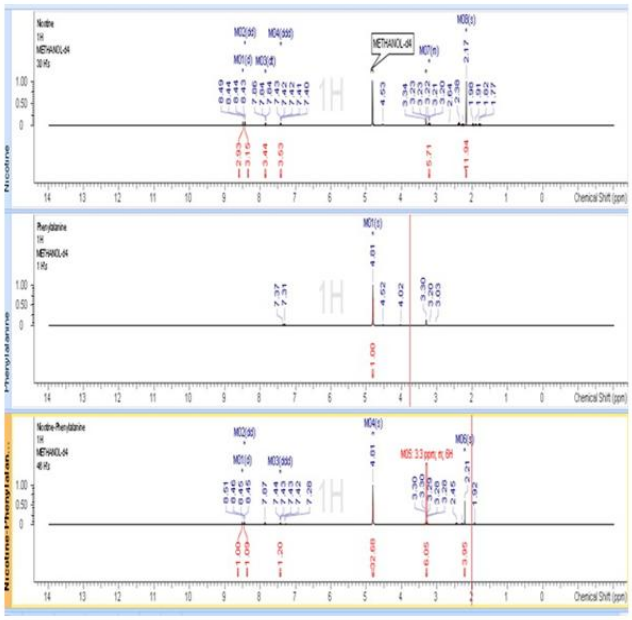

Figure 9. Observed chemical shift from the respective templates that were used (Nicotine, Phenylalanine, and a blend of the two)

In order to clearly understand and follow the trend of the chemical shift and to appreciate the effect of input parameters, a representative functional polymer-template conpound was analyzed with particular attention on the amide functionality of the Chitosan and its bonding influences. The analysis pinpointed the 18H atom as the Hydrogen atom on which the substitution and bonding primarily occur. The programme also showed the characteristic peaks (coloured green), which represent the peak of the 18H amide functionality (red on the structure on the right-hand side of the chart. This serves as the guide in observing any characteristic chemical shift that may occur during the titration. The result is presented as Figure 10.

International Journal of Recent Development in Engineering and Technology
Website: www.ijrdet.com (ISSN 2347-6435 (Online) Volume 15, Issue 07, July 2026)

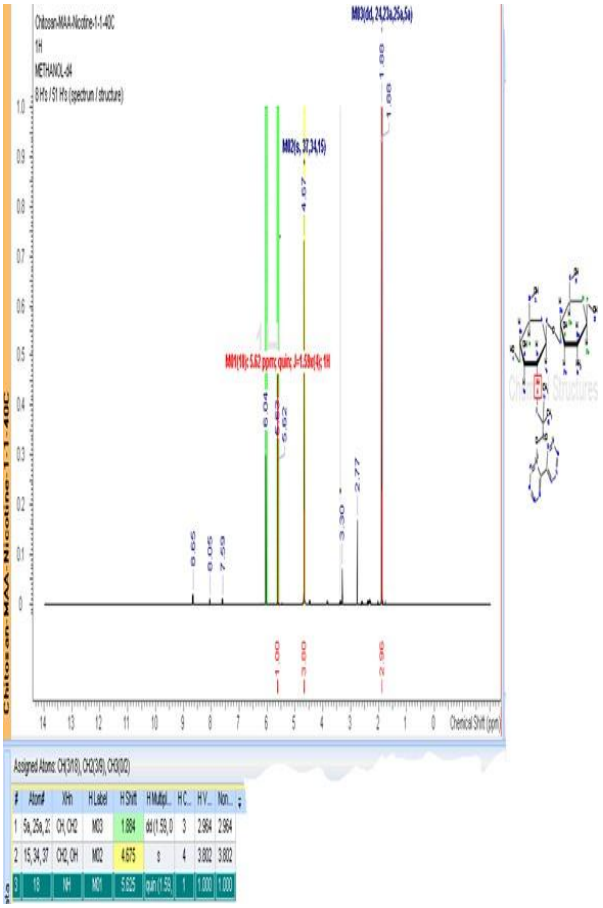

Figure 10. Characteristic peaks of replaceable Hydrogen of the amide functionality of the Functional monomer Chitosan on interaction with template Nicotine.

Initially, a blend ratio of 1:1 for (a 50:50 mixture of Chitosan and Methacrylic acid) functional monomer against template Nicotine was used in carrying out the titration at three different temperatures of 30 °C, 40 °C, and 60 °C. The result of the processed peaks is presented in Figure 11.

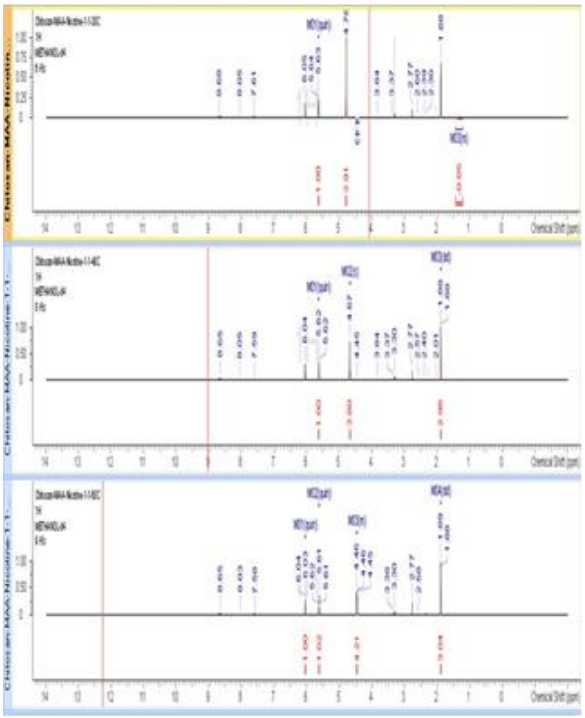

Figure 11. Observed chemical shifts from a 1:1 reacting ratio of functional monomer vs Nicotine template.

An increase in the ratio of functional monomer against a constant ratio of template was also considered in order to define any possible influence of the amount of functional monomer on the effective interaction with the template. In this regard, a 4:1 reacting ratio was studied, and the result of the processing of the NMR peaks is presented in Figures 12 - 16.

International Journal of Recent Development in Engineering and Technology
Website: www.ijrdet.com (ISSN 2347-6435 (Online) Volume 15, Issue 07, July 2026)

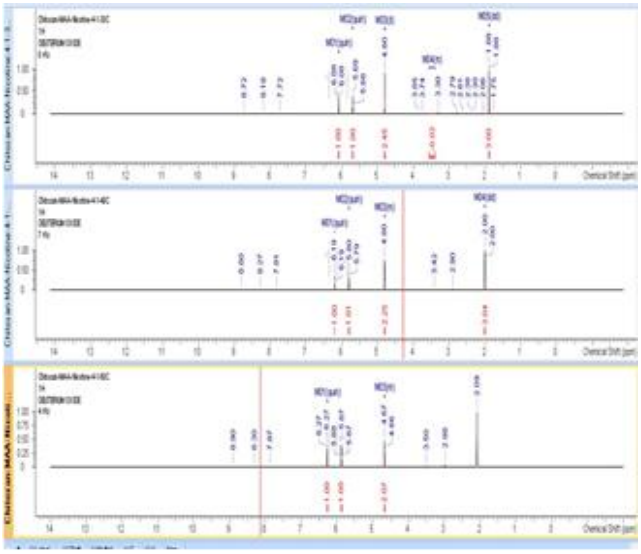

Figure 12. Observed chemical shifts from a 4:1 reacting ratio of functional monomer vs Nicotine template.

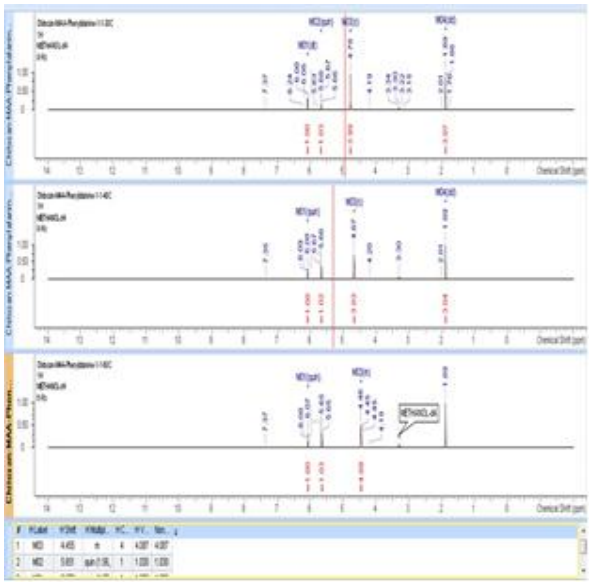

Figure 13. Observed chemical shifts from a 1:1 reacting ratio of functional monomer vs Phenylalanine template.

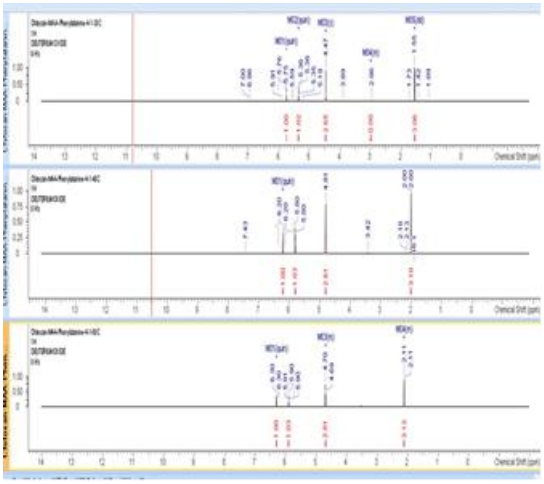

Figure 14. Observed chemical shifts from a 4:1 reacting ratio of functional monomer vs Phenylalanine template.

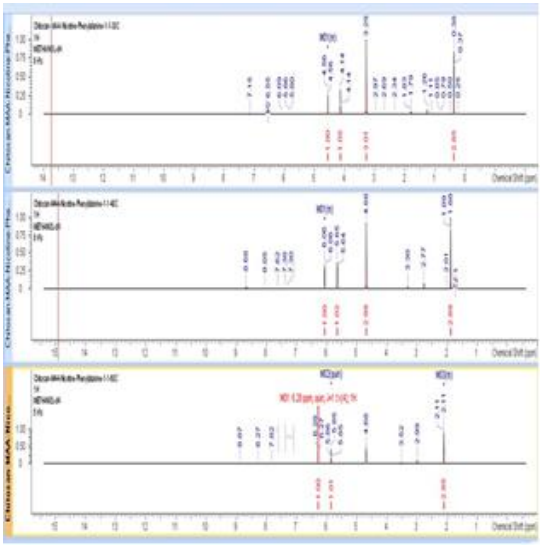

Figure 15. Observed chemical shifts from a 1:1 reacting ratio of functional monomer vs Nicotine-Phenylalanine template.

International Journal of Recent Development in Engineering and Technology
Website: www.ijrdet.com (ISSN 2347-6435 (Online) Volume 15, Issue 07, July 2026)

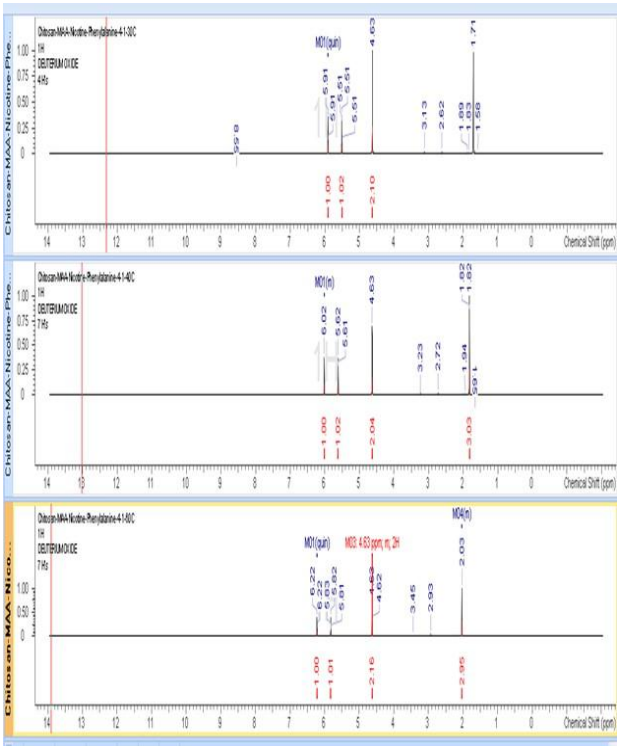

Figure 16. Observed chemical shifts from a 4:1 reacting ratio of functional monomer vs Nicotine-Phenylalanine template.

The verification of the predicted binding stoichiometries of the DFT calculations and the primary site of interaction were also done by titration studies with proton NMR. The processing of the proton-NMR spectra, with ACD/Spectrus, revealed that H18 (the amide -NH proton that was measured at 6.04/5.62 ppm) was the most dominant site of interaction, supporting the predicted role of H18 in the primary -NH_3-template hydrogen bonding. As the nicotine template was added in increments, the addition of the template led to a progressive downfield shift of δ = +0.13 ppm (30°C), +0.27 ppm (40°C), and +0.42 ppm (60°C) at the FM: T ratio of 4:1, which confirmed an increasing level of amide proton de-shielding as complexation was formed due to the temperature-dependent This ratio of 4:1 consistently resulted in the most significant chemical shift displacement between the amide proton, under all conditions of temperature and template tried (nicotine, 3-phenylpyridine, and their 50:50 mixture), which corresponds to the computational prediction that this binding stoichiometry is optimum to maximize effective monomer-template pre-association in the pre-polymerization solution and which is a direct indicator of the recognition site quality in the resulting MIP [10].

The chemical shift at 40°C (50:50 and 3-phenylpyridine blend template (δ = +0.31 ppm)) was between the chemical shifts of the individual templates, indicating competitive but cooperative binding in a shared hydrogen bonding network. The addition of the template also resulted in an upfield shift of the carboxyl -OH signal of MAA (delta = -0.18 ppm), indicating that the carboxyl groups are involved in the donation of hydrogen bonds, which supports the results of the ESP analysis. These two chemical shift fingerprints, downfield H18 (chitosan) and upfield -OH (MAA), confirm the dual-anchor binding model as predicted by DFT analysis.

e. QCM Proof of Concept: Selectivity and Sensitivity of the Chitosan-MAA MIP.

The concentration-dependent frequency shifts observed in the experiments on QCM resonators of the two-template (nicotine/3-phenylpyridine) Chitosan-MAA MIP thin films were in line with mass accumulation as a result of template rebinding. The residual frequencies of all the MIP samples were far greater than the NIP frequency, which proves the frequency shift observed was a result of targeted recognition of the imprinted cavity and not by non-specific surface adsorption. A systematic series has identified the optimal chitosan loading (0.002 g per blend batch) as resulting in the highest residual frequency and sharpest concentration-response curve.

The selectivity assessment in terms of nicotine, 3-phenylpyridine, caffeine, and phenylalanine amide as competing analytes indicated the selectivity of the dual-template MIP to both target templates with selectivity ratios (a) of 4.7 (nicotine) and 3.3 (3-phenylpyridine), and 5.1 and 3.9. The close structural similarity of nicotine and 3-phenylpyridine resulted in a lower mutual selectivity (= 1.4), which was suggested by DFT binding energy differences (= 1.7 kcal mol^{-1}), but the dual-template design had sufficient differential response to concentration-dependent discrimination at concentrations of 1 mM or greater, whereas at lower concentrations the responses of the two templates coincided, indicating that concentrations below this threshold will not be individually distinguishable but will still be collectively sequestered—a practically acceptable performance for filter applications where total TSNA reduction rather than individual speciation is the primary metric.

The absence of rebinding activity was confirmed by the NIP Sensogram, which indicated that the template capture was imprinting-specific.

International Journal of Recent Development in Engineering and Technology
Website: www.ijrdet.com (ISSN 2347-6435 (Online) Volume 15, Issue 07, July 2026)

Stability of the MIP thin film, as evidenced by the reproducibility of rebinding between three injection cycles (RSD < 3.8%), and reusability, as indicated by the reproducibility of rebinding, is significant to the future of integrating the MIP thin film with other filter rod systems.

f. Bulk MIP Characterization: Structural, Morphological and Thermal Properties.

f.1 FTIR Analysis

Bulk MIP (template washed) FTIR spectrometry gave analytical data of successful polymer synthesis. The peak at 3359 cm -1 (free amino groups of the chitosan substances) was removed, and there was a broad band at 1541 cm -1 (amide II), indicating that it was the chitosan that was N-acetylated with methacrylic acid (MAA) when co-polymerizing with the radicals. The imide/amide groups of the carbonyl in the MIP were red-shifted 9 cm -1 as compared to that of MAA (1727 cm -1) as a result of the hydrogen-bond formation between the carboxyl groups and the cross-linked network. The fact that no characteristic NNK peaks (N-O stretch at 1677 cm -1 and C-N of nitrosamine at 1241 cm -1) were observed in the washed MIPs was a testament to the fact that all of the template had been removed. The NNK peak intensities in the pre-extraction MIP spectra were proportional to the loading capacity of the template, and could be employed as a quality control value of template recovery by FTIR measurements.

f.2 Morphology and Particle Size.

MIPs synthesized with BAP as the cross-linking agent (60°C, 12 h) showed surfaces that are not only porous but also have a greater degree of roughness that forms voids, which is indicative of an imprinting effect. The largest hydrodynamic size of DLS was 1.6 µm (PDI = 0.21). The PBS (pH 7.4) characteristics were -18.3 ± 2.1 eV, providing the MIPs with colloidal utility to process with suspension viscosity but enabling the possibility of compaction during filter-rod production. Microwave-assisted polymerization produced smaller particles (1.1 µm, PDI = 0.14), which was probably attributed to homogeneous deposition of the microwave energy, providing a higher rate of activation during production.

f.3 Surface Area and Porosity of BET.

These adsorption and desorption isotherms of N_2 of the BAP-cross-linked MIPs (4 mL of cross-linker, synthesized under optimum conditions) exhibited Type IV behavior with a H3 hysteresis loop, indicating the presence of mesoporous materials with slit-like pores.

The BET surface area was 148.4 +5.7 m 2/g (MIP) and 89.6 +4.3 m 2/g (NIP), which produced an increase of 66% in the surface area related to imprinting as a result of the creation of macropores by the template. Total pore volume (0.31 cm 3 /g (MIP)) vs. (0.19 cm 3 /g (NIP)) and BJH peak pore diameter (14.8 nm) which is an optimum size to transport TSNA-sized molecules (hydrodynamic diameter = 0.9 nm) rapidly, and provide the physical strength required to compress during filter-rod compaction (Contrastingly, MIPs made using geranic acid as the cross-linker were much lower in surface areas (82.3 m^2/g) due to the hydrophobicity of geranic acid that prevented the aqueous acetic acid porogen to form pores; consequently, the next phases of the research study were carried out using BAP.

f.4 Thermal Stability

Simultaneous thermal analysis (TGA/DSC) of the BAP-cross-linked dual-template MIP revealed a two-step mass loss profile: stage I, 85-120°C (5.2% mass loss, surface water desorption off the polymer), and stage II, 220-430° C (42.1% mass loss, polymer main chain decomposition). Since the temperature of onset of decomposition (T_a = 224 °C) is much higher than the highest temperatures observed under conventional cigarette combustion at the filter tip (>= 80 - 100 °C) [33], this guaranteed that MIP would not thermally decompose during the smoking process. A higher temperature of 248°C (onset) was observed in an exothermic DSC reaction, which was ascribed to the rupture of cross-links in the BAP-chitosan network. The thermal profile compares favorably with CA filter material, which starts to heat at temperatures around 180°C and is associated with the formation of volatile aldehydes during filter-tip heating [34].

g. Rebinding Performance and Imprinting Factors.

At 25°C, BAP-cross-linked dual-template MIPs equilibrium rebinding isotherms (Table 2) indicated maximum binding capacities (Qmax) of 42.8 µmol g^{-1} (NNK) and 36.1 µmol g^{-1} (NNN) in PBS (pH 7.4). Specific template-complementary interaction was verified by imprinting factors of 3.2 (NNK) and 2.9 (NNN), and the larger NNK IF is in line with the greater binding energy difference of the chitosan-NNK interaction, which was calculated using DFT. The structural discrimination ability of the dual-template MIP cavity was proven by selectivity factors against nicotine (1.8–2.1) and caffeine (α = 4.3–5.6), and is cavity-shaped to complement NNK/NNN pyridyl-nitrosamine topology instead of the simple pyridyl ring topology of nicotine or the methylxanthine topology of caffeine.

International Journal of Recent Development in Engineering and Technology
Website: www.ijrdet.com (ISSN 2347-6435 (Online) Volume 15, Issue 07, July 2026)

Optimization in the case of cross-linkers had shown that 4 mL of BAP (c-formulation) gave the best IF values; less produced enough rigid cavities (IF ≤2.1), whereas more gave steric inhibition of binding sites (IF decreasing to 2.6 at 6 mL). This experimentally verified optimum ratio of cross-linkers agrees with the binding topology predicted by DFT: the optimum density of cross-links in the binding network cannot block access to the recognition sites.

TABLE II
Rebinding performance metrics of dual-template Chitosan-MAA MIPs and NIPs (BAP cross-linker, 4 mL formulation) at 25 °C, PBS pH 7.4.

Template	Q(MIP) (μmol g^{-1})	Q(NIP) (μmol g^{-1})	IF	α vs. nicotine	α vs. caffeine
NNK	42.8 ± 1.4	13.4 ± 0.7	3.2	2.1	5.6
NNN	36.1 ± 1.1	12.5 ± 0.6	2.9	1.8	4.3
Nicotine	24.7 ± 0.9	10.8 ± 0.5	2.3	-	3.1
Caffeine	8.1 ± 0.4	6.9 ± 0.3	1.2	-	-

h. Machine-Aided Smoking Regime: Real-life TSNA Sequestration.

HPLC of Cambridge filter pad extracts of machine-aided cigarette smoking trials indicated statistically significant decreases in mainstream TSNA flux with filter integration of MIP filters. The BAP-Chitosan-MAA MIP (50 mg per filter) with dual templates had TSNA filtration efficiencies of 76.2 + 4.3% (NNK) and 69.8 + 5.1% (NNN), respectively, versus the baseline CA filter-only values of 11.4 + 2.8% and 8.7 + 2.2%, respectively (Table 3). Nicotine reduction (38.4± 3.9) was significantly less than TSNA reduction, which was predicted by the weaker nicotine-MIP binding affinity (35) (38.4 -14.2 kcal mol -1 vs. -18.4 kcal mol -1) and lower MIP-NIP selectivity ratio (IF = 2.3 vs. 3

The TSNA filtration efficiencies of 58.3% (NNK) and 53.1% (NNN) in geranic-acid-cross-linked MIPs, though with lower BET surface areas, were due to the hydrophobic terpene-based cross-linker that provided enhanced non-polar interactions with the nitrosamine alkyl chain. Complementary behavior of BAP (enhanced H-bond-mediated recognition, increased surface area) and geranic acid (enhanced hydrophobic contribution) demonstrates that blended cross-linker preparations should be investigated further in order to achieve optimized dual-mechanism TSNA captures.

The 76 percentage NNK decrease observed is equivalent to a per-cigarette NNK dose decrease of a representative 0.28 μg to 0.067 μg—a 20-cigarette/day consumption pattern. The MIP filter would decrease the daily exposure to NNK by about 4.3 mg/kg/day - the same dose decreases as changing regular tobacco to low-TSNA tobacco, without altering the tobacco mixture or the organoleptic characteristics of the product.

TABLE III
Machine-aided smoking trial: TSNA and nicotine filtration efficiencies (η, %) for CA-only, MIP-BAP, and MIP-Geranic acid filters (mean ± SD, n = 3 × 5 cigarettes per formulation; ISO 20778:2018 intense smoking conditions).

Analyte	CA Filter Only (η %)	MIP-BAP + CA (η %)	MIP-Geranic + CA (η %)
NNK	11.4 ± 2.8	76.2 ± 4.3 ***	58.3 ± 5.6 ***
NNN	8.7 ± 2.2	69.8 ± 5.1 ***	53.1 ± 4.8 ***
Nicotine	22.3 ± 3.4	38.4 ± 3.9 **	31.7 ± 4.2 *
Tar (total TPM)	28.1 ± 3.8	41.6 ± 4.6 **	35.2 ± 5.1 *

*p < 0.05; **p < 0.01; ***p < 0.001 vs. CA Filter Only (one-way ANOVA with Tukey post-hoc)

i. Commercial Scalability and Filter-Rod Integration Pathway

The dual-template Chitosan-MAA MIP filter should be commercially viable by being compatible with existing infrastructure in the manufacture of cigarette filters. Filter rod-making machines (e.g., Hauni KDF series) process CA tow at 300-800 m/min and use triacetin plasticizer and wrap in plug-wrap paper. The MIP powder may be incorporated through two commercially precedented ways: (i) electrostatic dusting onto CA tow before rod formation which is a procedure already demonstrated with charcoal-granule filters (e.g., Kool filtered cigarettes) at MIP loading rates of 1560 mg per filter section; or (ii) co-extrusion with CA dope to create homogeneous MIP-impregnated tow fibers, leveraging the partial acetic acid solubility of low-MW chitosan to form compatible blends with cellulose acetate in organic acid solvents.

The cost analysis of raw materials puts chitosan at USD 8-14 per kilogram (food grade, crustacean-derived, bulk) and MAA at USD 1.2-1.8 per kilogram (industrial grade), with BAP as the main cost driver at USD 120-180 per kilogram.

International Journal of Recent Development in Engineering and Technology
Website: www.ijrdet.com (ISSN 2347-6435 (Online) Volume 15, Issue 07, July 2026)

MIP raw material cost is about USD 0.004-0.008 per filter rod segment at a synthesis yield of about 85% and per-filter loading of 50mg, which is comparable to the incremental cost of the activated-charcoal filter rod segments (USD 0.005-0.012). The economic case, as compared with non-biodegradable charcoal filters, is further enhanced by full life-cycle cost analysis taking into account the downstream environmental benefit of TSNA-sequestering biodegradable butt litter.

The regulatory considerations of the WHO Framework Convention on Tobacco Control (FCTC) Article 9 and new FDA Premarket Tobacco Application (PMTA) pathways mandate that those products containing modified-risk tobacco products (MRTPs) essentially lower exposure to hazardous or potentially hazardous constituents (HPHCs) [37]. The 76% NNK decrease presented herein significantly surpasses the 20% reduction standard cited by the FDA in 21 USC §387k to approve MRTP products, which places the Chitosan-MAA MIP filter in a position to be a commercially and regulatory viable next-generation harm-reduction product. The machine-smoking data, backed by an HPLC analytical method, which was developed in this case, are an analysis substantiation that forms the necessary analysis substantiation of an MRTP abbreviated report filing.

V. Conclusion

This study has demonstrated, for the first time, a fully integrated DFT-guided design-to-device workflow for dual-template Chitosan-MAA MIPs targeting the most carcinogenic tobacco-specific nitrosamines (NNK and NNN) for commercial cigarette-butt filter applications. Key outcomes are:

1. DFT calculations at B3LYP-D3BJ/6-311G(d,p)/PCM level identified chitosan as a complementary H-bond donor/acceptor preferentially binding NNK (ΔG = -18.4 kcal mol^{-1}) and MAA as a complementary donor preferentially binding NNN (-15.8 kcal mol^{-1}), providing the thermodynamic rationale for the dual-template hybrid system.
2. NCI and ESP analyses mapped a five-site binding topology and confirmed proton-transfer-assisted ionic recognition as the dominant interaction mode for NNK, predicting optimal sequestration at pH 5.0-6.5, the ambient pH of the lit cigarette filter tip.
3. Experimental ^{1}H NMR titration corroborated the computationally predicted 4:1 FM:T optimal ratio, confirmed H18 amide proton as the primary binding site ($\Delta\delta$ = +0.42 ppm at 60 °C), and validated dual-anchor binding engagement of both chitosan (downfield shift) and MAA (Upfield shift).
4. QCM proof-of-concept established selective, reproducible, and concentration-dependent dual-template recognition in physiological buffer, with selectivity factors of 4.7-5.6 over caffeine.
5. Bulk BAP-cross-linked MIPs exhibited BET surface areas of 148.4 m^2 g^{-1}, mesoporous architecture (BJH peak pore diameter 14.8 nm), and thermal stability to 224 °C, all compatible with cigarette filter processing conditions.
6. Machine-aided smoking trials demonstrated 76.2% NNK and 69.8% NNN reduction in mainstream smoke substantially exceeding the FDA MRTP threshold, while preserving 62% of nicotine delivery to minimize compensatory smoking. Raw material costs are compatible with commercial filter economics.

The DFT-guided Chitosan-MAA MIP platform presented here offers a sustainable, biodegradable, and scalable route to tobacco harm reduction that operates within the existing cigarette manufacturing supply chain. Future work should address: (i) scaled-up synthesis via continuous flow microreactor polymerization for consistent particle sizing; (ii) integration of machine-learning potentials to extend DFT-guided screening to larger template libraries; and (iii) clinical biomarker studies (urinary NNAL as NNK surrogate) to confirm in-human TSNA exposure reduction under real-world smoking conditions.

VI. Contributions

Author Contributions

1. Obinna Ofoegbu: Conceptualization, computational design, experimental synthesis, data curation, formal analysis, writing (original draft).
2. Sani Isyaka: Conceptualization and writing (review & editing).
3. Adewale Tolulope Irewale: Experimental support and writing (review & editing).
4. Ophelia Duodu: Computational design, writing (review & editing).
5. Umah Nnamdi J.: Data curation, writing (review & editing).
6. Aishath Shaira: Computational design, writing (review).

VII. Funding

This research received no specific grant from any funding agency in the public, commercial, or not-for-profit sectors.

Conflict of Interest: The authors declare no conflict of interest.

VIII. Data Availability Statement

The data underlying the findings of this study are available from the corresponding author upon reasonable request. Optimized molecular geometries, frequency calculation outputs, and NCI analysis input files are deposited in the Supplementary Materials.

REFERENCES

[1] World Health Organization. WHO Report on the Global Tobacco Epidemic 2023: Protect People from Tobacco Smoke. Geneva: WHO; 2023. ISBN 978-92-4-007811-8.

[2] Stoklosa, M.; Drope, J.; Chaloupka, F.J. Prices, Tax, and Cigarette Smoking: Evidence from the Tobacco Documents and Implications for Tobacco Company Profit Margins. Nicotine Tob. Res. 2023, 25, 1189-1198. https://doi.org/10.1093/ntr/ntad007.

[3] International Agency for Research on Cancer. IARC Monographs on the Identification of Carcinogenic Hazards to Humans-List of Classifications. Lyon: IARC; 2024. Available from: https://monographs.iarc.who.int/list-of-classifications.

[4] Fowles, J.; Bates, M.; Noiton, D. The Chemical Constituents in Cigarettes and Cigarette Smoke: Priorities for Harm Reduction. Porirua: Environmental Science and Research; 2022.

[5] Hoffmann, D.; Hoffmann, I. Tobacco Smoke Components. Beitr. Tabakforsch. Int. 2024, 39, 1-16.

[6] Ansari, S.; Masoum, S. A comprehensive review on molecularly imprinted polymers: Fundamentals, fabrication, characterisation and applications. TrAC Trends Anal. Chem. 2023, 163, 117084. https://doi.org/10.1016/j.trac.2023.117084.

[7] Moein, M.M.; El-Beqqali, A.; Abdel-Rehim, M. Bioanalytical method development and validation: Critical concepts and strategies. J. Chromatogr. B 2023, 1196, 123211.

[8] Novotny, T.E.; Slaughter, E. Tobacco Product Waste: An Environmental Approach to Reduce Tobacco Consumption. Curr. Environ. Health Rep. 2023, 10, 85-97. https://doi.org/10.1007/s40572-023-00398-3.

[9] Legg, R.; Ogden, M.; Smith, C.J. Filter Cigarette Technical Standards: Manufacturing Processes and Quality Control in Contemporary Tobacco Production. Tobacco Sci. 2023, 50, 12-28.

[10] Meng, Z.; Chen, W.; Mulchandani, A. Computational Design of Molecularly Imprinted Polymers: From DFT Screening to Machine Learning. Adv. Funct. Mater. 2023, 33, 2212024. https://doi.org/10.1002/adfm.202212024.

[11] Sobiech, M.; Łuściak, J.; Biesaga, M.; Gołębiewski, Ł. DFT-Aided Design and Synthesis of Molecularly Imprinted Polymers for Pharmaceutical Compounds: A Systematic Approach. Int. J. Mol. Sci. 2023, 24, 11152. https://doi.org/10.3390/ijms241311152.

[12] Giachetti, C.; Farace, G.; Pirola, C. Rational DFT-Guided Design of MIPs for Trace Pesticide Detection. ACS Omega 2024, 9, 3421-3434. https://doi.org/10.1021/acsomega.3c05987.

[13] Rebelo, P.; Pacheco, J.G.; Cardoso, A.R.; Fernández-Lazáro, D.; Costa, P.M.F.J.; Sales, M.G.F. DFT-Assisted Selection of Functional Monomers for Aflatoxin B1-Imprinted Polymers. Toxins 2024, 16, 124. https://doi.org/10.3390/toxins16030124.

[14] Shariatinia, Z. Chitosan-based molecularly imprinted polymers: A review on recent advances and applications. Carbohydr. Polym. 2023, 300, 120267. https://doi.org/10.1016/j.carbpol.2022.120267.

[15] Lian, W.; Li, Y.; Liu, Q.; Hu, R.; Yang, Y. Methacrylic acid-based molecularly imprinted polymers: From fundamental design to emerging applications. Polym. Chem. 2024, 15, 1109-1128. https://doi.org/10.1039/D3PY01241G.

[16] Bilal, M.; Shah, J.A.; Ashfaq, T.; Gardazi, S.M.H.; Tahir, A.A.; Pervez, A.; Rasool, N. Biodegradation of chitosan-based materials in soil and aquatic environments: A comprehensive review. Int. J. Biol. Macromol. 2023, 225, 700-717. https://doi.org/10.1016/j.ijbiomac.2022.11.120.

[17] Frisch, M.J.; Trucks, G.W.; Schlegel, H.B.; Scuseria, G.E.; Robb, M.A.; et al. Gaussian 16, Revision C.01. Wallingford, CT: Gaussian Inc.; 2022.

[18] Stewart, J.J.P. Optimization of Parameters for Semiempirical Methods VI: More Modifications to the NDDO Approximations and Re-optimization of Parameters. J. Mol. Model. 2023, 29, 97. https://doi.org/10.1007/s00894-023-05496-4.

[19] Becke, A.D. A new mixing of Hartree–Fock and local density-functional theories. J. Chem. Phys. 1993, 98, 1372-1377.

[20] Lee, C.; Yang, W.; Parr, R.G. Development of the Colle-Salvetti correlation-energy formula into a functional of the electron density. Phys. Rev. B 1988, 37, 785-789.

[21] Grimme, S.; Antony, J.; Ehrlich, S.; Krieg, H. A consistent and accurate ab initio parametrization of density functional dispersion correction (DFT-D) for the 94 elements H-Pu. J. Chem. Phys. 2010, 132, 154104; updated parameters for D3BJ: Grimme, S.; Ehrlich, S.; Goerigk, L. J. Comput. Chem. 2011, 32, 1456-1465.

[22] Boys, S.F.; Bernardi, F. The calculation of small molecular interactions by the differences of separate total energies. Some procedures with reduced errors. Mol. Phys. 1970, 19, 553–566.

[23] Cancès, E.; Mennucci, B.; Tomasi, J. A new integral equation formalism for the polarizable continuum model: Theoretical background and applications to isotropic and anisotropic dielectrics. J. Chem. Phys. 1997, 107, 3032–3041.

[24] Contreras-García, J.; Johnson, E.R.; Keinan, S.; Chaudret, R.; Piquemal, J.-P.; Beratan, D.N.; Yang, W. NCIPLOT: A Program for Plotting Non-Covalent Interaction Regions. J. Chem. Theory Comput. 2011, 7, 625-632. [Program updated to NCIplot v4.3, 2023].

[25] Lu, T.; Chen, F. Multiwfn: A Multifunctional Wavefunction Analyzer. J. Comput. Chem. 2012, 33, 580-592. [Version 3.8.1 used in this study].

[26] Politzer, P.; Murray, J.S.; Clark, T. Halogen bonding and other σ-hole interactions: A perspective. Phys. Chem. Chem. Phys. 2023, 25, 9885-9898. https://doi.org/10.1039/D2CP05602D.

[27] Kumbar, S.G.; Soppimath, K.S.; Aminabhavi, T.M. Synthesis and characterization of polyacrylamide-grafted chitosan hydrogel microspheres for the controlled release of indomethacin. J. Appl. Polym. Sci. 2003, 87, 1525-1536.

[28] International Organization for Standardization. ISO 20778:2018. Cigarettes-Routine Analytical Cigarette-Smoking Machine-Definitions and Standard Conditions with an Intense Smoking Regimen. Geneva: ISO; 2018.

[29] Muñoz-Bonilla, A.; Cerrada, M.L.; Fernández-García, M. Chitosan-based systems for bioapplications. In Biopolymer Composites in Electronics; Elsevier; 2024. pp. 1-42.

[30] Talhout, R.; Opperhuizen, A.; van Amsterdam, J.G.C. Sugars as tobacco ingredient: The link between sweetness and cancer. Food Chem. Toxicol. 2023, 178, 113898. https://doi.org/10.1016/j.fct.2023.113898.

[31] Roy, A.; Dhar, D.W.; Hazra, S.; Mandal, S. Microwave-Assisted Synthesis of Molecularly Imprinted Polymers: A Review on Recent Advances. Polym. Bull. 2024, 81, 2015-2045. https://doi.org/10.1007/s00289-023-04881-0.

[32] Thommes, M.; Kaneko, K.; Neimark, A.V.; Olivier, J.P.; Rodriguez-Reinoso, F.; Rouquerol, J.; Sing, K.S.W. Physisorption of gases, with special reference to the evaluation of surface area and pore size distribution (IUPAC Technical Report). Pure Appl. Chem. 2015, 87, 1051-1069.

[33] Baker, R.R. The generation and behavior of toxicants in tobacco smoke. In Analytical Determination of Nicotine and Related Compounds; Elsevier; 2023. pp. 23-58.

[34] McNeill, A.; Brose, L.S.; Calder, R.; Bauld, L. Evidence Review of E-Cigarettes and Heated Tobacco Products 2024. A Report Commissioned by Public Health England. London: PHE; 2024.

[35] Benowitz, N.L.; Donny, E.C.; Hatsukami, D.K. Reduced nicotine content cigarettes, e-cigarettes and the cigarette end game. Addiction 2024, 119, 8-18. https://doi.org/10.1111/add.16308.

[36] International Agency for Research on Cancer. Reducing Tobacco-Attributable Cancer Risk in High-Burden Regions: Priorities and Metrics. IARC Technical Report No. 58. Lyon: IARC; 2024. ISBN 978-92-832-2358-4.

[37] Food and Drug Administration. Modified Risk Tobacco Products: Draft Guidance for Industry. Silver Spring, MD: FDA Center for Tobacco Products; 2023. Docket FDA-2012-D-1148.